Appendix

I Summary of Preparation Parameters

I.i Preparation of the Spraying Solutions

Table I.1: Preparation of the spaying solutions that were used for the Spray ILGAR deposition of the investigated thin films in the course of this thesis. For all copper-containing solutions, Copper (II) hexafluoroacetylacetonate hydrate (Cu(hfac)$_2$; Strem Chemicals, Inc.; 99 %) was used as a copper source. For all indium-containing solutions, Indium (III) chloride ($InCl_3$; Alfa Aesar GmbH & Co KG; 99.99 %) was used as an indium source. “THF” stands for tetrahydrofuran.

Sample No.	Solvent	Amount of Cu(hfac)$_2$ solution [ml]	Concentration of Cu(hfac)$_2$ solution [mMol]	Amount of $InCl_3$ solution [ml]	Concentration of $InCl_3$ solution [mMol]	[Cu]:[In] ratio of the mixed solution	Remarks
301	Ethanol	25	10	0	0	∞	
302	Ethanol	25	10	0	0	∞	
303	Ethanol	25	10	0	0	∞	
304	Ethanol	25	10	0	0	∞	
305	Ethanol	25	10	0	0	∞	
306	Water	25	10	0	0	∞	
307	Isopropanol	25	10	0	0	∞	
308	Ethanol	25	10	0	0	∞	
309	Acetonitrile	25	10	0	0	∞	
310	THF	25	10	0	0	∞	
311	Acetone	25	10	0	0	∞	
312	Acetone	25	10	0	0	∞	
313	Acetone	25	10	0	0	∞	
314	Acetone	25	10	0	0	∞	
315	Acetone	25	10	0	0	∞	
316	Acetone	25	10	0	0	∞	
317	Acetone	25	10	0	0	∞	
318	Acetone	25	10	0	0	∞	
319	Acetone	25	10	0	0	∞	
320	Acetone	25	10	0	0	∞	
321	Acetone	25	10	0	0	∞	
322	Acetone	25	10	0	0	∞	
323	Acetone	25	40	0	0	∞	
324	Acetone	0	0	25	40	0	
325	Acetone	25	40	25	40	(1)	Separate Cu(hfac)$_2$ and $InCl_3$ solutions
326	Acetone	25	40	25	40	(1)	
327	Acetone	25	40	25	40	(1)	
328	Acetone	25	40	25	32	(1.25)	
329	Acetone	25	40	25	40	1	
330	Acetone	25	40	20	40	1.25	
401	Acetone	12.5	40	0	0	∞	

Sample No.	Solvent	Amount of $Cu(hfac)_2$ solution [ml]	Concentration of $Cu(hfac)_2$ solution [mMol]	Amount of $InCl_3$ solution [ml]	Concentration of $InCl_3$ solution [mMol]	[Cu]:[In] ratio of the mixed solution	Remarks
402	Acetone	0	0	25	40	0	
403	Acetone	25	40	20	40	1.25	
404	Acetone	12.5	40	10	40	1.25	
405	Acetone	12.5	40	10	40	1.25	
406	Acetone	12.5	40	10	40	1.25	
407	Acetone	1-2	40	0	0	∞	
408	Acetone	0	0	1-2	40	0	
409	Acetone	~1	40	<1	40	1.25	
410	Acetone	~1	40	<1	40	1.25	
411	Acetone	25	40	20	40	1.25	+2 ml H_2O
412	Acetone	12.5	40	10	40	1.25	
413	Acetone	25	40	20	40	1.25	
414	Acetone	25	40	16.6	40	1.5	
415	Acetone	25	40	14.3	40	1.75	
416	Acetone	25	40	12.5	40	2	
417	Acetone	25	40	14.3	40	1.75	
418	Acetone	25	40	20	40	1.25	
419	Acetone	25	40	26	40	0.95	
420	Acetone	25	40	26	40	0.95	
421	Acetone	25	40	26	40	0.95	
422	Acetone	15	40	10	40	1.5	+1 ml H_2O
601	Acetone	62.5	40	50	40	1.25	
602	Acetone	75	40	60	40	1.25	
603	Acetone	100	40	80	40	1.25	
604	Acetone	50	40	54	40	0.93	

I.ii Preparation Parameters of the Spray ILGAR Process

Table I.2: Preparation parameters of the Spray ILGAR process that were used for the Spray ILGAR deposition of the investigated thin films in the course of this thesis. The Ar/H_2S reactant gas flow rate was held constant at 1.3 l/min in all experiments. All process steps of the ILGAR-cycle were separated by breaks of 10 s, in which the reaction chamber was purged with N_2, which was running throughout the entire process at a constant rate (this table). For all samples, 2.5x2.5x0.2 cm^3 soda-lime glass substrates covered by a sputtered 0.5-1µm molybdenum cover layer were used.

Sample No.	Nitrogen flow rate [l/min]	Substrate temperature [°C]	Aerosol preheating temperature [°C]	Spray step duration [s]	H_2S step duration [s]	Number of ILGAR-cycles	Remarks
301	5.5	250	No preheating	10	20	30	
302	5.5	350	No preheating	10	20	31	
303	5.5	400	No preheating	10	20	35	
304	5.5	400	No preheating	30	20	18	
305	5.5	430	No preheating	30	20	22	
306	5.5	430	No preheating	No nebulization			
307	5.5	430	No preheating	No nebulization			
308	5.5	430	No preheating	30	20	22	
309	5.5	430	No preheating	30	20	16	
310	5.5	430	No preheating	30	20	14	
311	5.5	430	No preheating	30	20	9	
312	3.3	430	70	30	20	11	
313	3.3	430	100	30	20	10	
314	3.3	430	140	30	20	6	
315	3.3	430	150	30	20	6	
316	3.3	430	180	30	20	10	
317	3.3	430	200	30	20	10	

Sample No.	Nitrogen flow rate [l/min]	Substrate temperature [°C]	Aerosol preheating temperature [°C]	Spray step duration [s]	H_2S step duration [s]	Number of ILGAR-cycles	Remarks
318	1.1	430	100	30	20	29	
319	2.2	430	100	30	20	15	
320	3.3	430	100	30	20	10	
321	4.4	430	100	30	20	9	
322	5.5	430	100	30	20	8	
323	3.3	430	100	30	20	11	
324	3.3	430	100	30	20	14	
325	3.3	430	100	30	20	30	
326	3.3	430	100	30	20	27	
327	3.3	430	100	15+15	20	18	
328	3.3	430	100	15+15	20	19	
329	3.3	430	100	30	20	22	
330	3.3	430	100	30	20	24	
401	3.3	430	100	20	0	12	
402	3.3	430	100	30	0	16	
403	3.3	430	100	20	0	40	
404	3.3	430	100	60	60	8	
405	3.3	430	100	120	60	4	
406	3.3	430	100	240	60	2	
407	3.3	430	100	30	0	1	
408	3.3	430	100	30	0	1	
409	3.3	430	100	30	0	1	
410	3.3	430	100	30	0	1	
411	3.3	430	100	20	0	40	
412	3.3	430	100	30	40	14	
413	3.3	430	100	20	120	23	
414	3.3	430	100	30	20	25	
415	3.3	430	100	30	20	21	
416	3.3	430	100	30	20	23	
417	3.3	430	100	30	40	19	
418	3.3	430	100	30	60	25	
419	3.3	430	100	30	60	19	
420	3.3	430	100	30	60	20	
421	3.3	430	100	30	10	29	
422	3.3	430	100	30	40	18	
601	3.3	430	100	30	30	51	
602	3.3	430	100	30	30	65	
603	3.3	430	100	30	30	84	
604	3.3	430	100	30	10	60	

I.iii Parameters of the Post-Deposition Treatments

Table I.3: Preparation parameters of post-deposition treatments. The H_2S annealing was performed in a standard quartz tube oven using a 95 % Ar / 5 % H_2S gas mixture (Air Liquide). The KCN etching was performed according to a standard recipe described in Ref. [Weber '02]. In case of solar cell preparation, the cells were completed as described in Ref. [Klaer '03; Scheer '04; Klenk '05].

Sample No.	Duration of Ar annealing at 375 °C [min]	Duration of Ar annealing at 550 °C [min]	Duration of H_2S annealing at 550 °C [min]	KCN etching applied [Yes/No]	Solar cell preparation [Yes/No]	Remarks
325	45	0	15	Yes	No	
326	45	0	15	Yes	No	
327	45	0	15	Yes	No	
328	45	0	15	Yes	No	
329	45	0	15	Yes	No	

Sample No.	Duration of Ar annealing at 375 °C [min]	Duration of Ar annealing at 550 °C [min]	Duration of H_2S annealing at 550 °C [min]	KCN etching applied [yes/no]	Solar cell preparation [yes/no]	Remarks
330	45	0	15	Yes	No	
412	0	0	45	Yes	No	
413	0	0	45	Yes	No	
414	60	0	15	Yes	No	
415	60	0	15	Yes	No	
416	60	0	15	Yes	No	
417	60	0	15	Yes	No	
418	0	0	90	Yes	No	
419	0	0	30	No	No	
420	60	60	30	No	No	
421	60	60	30	No	No	KCN only for Raman analysis
422	60	60	60	No	No	
601	0	0	90	Yes	Yes	
602	0	0	90	Yes	Yes	
603	0	0	90	Yes	Yes	
604	60	60	60	Yes	Yes	

II List of Abbreviations

a-C	Amorphous carbon
a-C:H	Hydrogenated amorphous carbon
ALD	Atomic Layer Deposition
arb. u.	Arbitrary units
as-dep.	As-deposited
at. %	Atomic %
mol. %	Molar %
CuAu-ordered $CuInS_2$	CuAu I-type cation-ordered $CuInS_2$
$Cu(hfac)_2$	Copper hexafluoroacetylacetonate hydrate
$Cu_{2-\delta}S$	Copper sulfide phase: Digenite (Table 2.2)
$Cu_{2-x}S$	Blend of various copper sulfide phases with a stoichiometry close to [Cu]:[S] = 2 with $0 \leq x \leq 0.2$
CVD	Chemical Vapor Deposition
CVT	Chemical Vapor Transport
DLC	Diamond-like carbon
EDX	Energy-dispersive X-ray spectroscopy
ERDA	Elastic recoil detection analysis
ETHZ	Eidgenössisch Technische Hochschule Zürich
Fig.	Figure
FWHM	Full peak width at half of the maximum peak intensity
hfac	hexafluoroacectlacetonate group
HMI	Hahn-Meitner-Institut Berlin GmbH
ILGAR	Ion Layer Gas Reaction
ISL	Ionenstrahllabor
JCPDS	Joint Committee on Powder Diffraction Standards
JV-measurements	Current density vs. voltage measurements
NC-G	Nano-crystalline Graphite
Norm.	Normalized
pc	Polycrystalline
PCM	Phonon confinement model
PV	Photovoltaic energy conversion
PVD	Physical Vapor Deposition
QE	External quantum efficiency
Rel. u.	Relative units
RTP	Rapid Thermal Processing
sc	Single-crystalline
SCR	Space charge region
SEM	Scanning electron microscopy
ta-C	Tetrahedral amorphous carbon
ta-C:H	Hydrogenated tetrahedral amorphous carbon
TEM	Transmission electron microscopy
THF	Tetrahydrofuran
XAS	X-ray Auger spectroscopy
XPS	X-ray photoelectron spectroscopy
XRD	X-ray diffraction
XRF	X-ray fluorescence analysis
I-III-VI_2	Chalcopyrite compound consisting of one atom of group I of the periodic system, one atom of group III, as well as two atoms of group VI.

III List of Symbols

General notation of symbols:

X	Notation for a constant
X	Notation for a variable scalar
$\boldsymbol{X}$	Notation for a variable vector
$\underline{\boldsymbol{X}}$	Notation for a variable tensor
$\langle X \rangle$	Notation for the average value of parameter X

Symbols used in this thesis:

A	Diode quality factor
a, b, c	Lattice constants of the unit cell of a crystal lattice
d	Mean droplet diameter of aerosol droplets
c	Concentration
c	Speed of light: $2.9979 \cdot 10^{8}$ m s^{-1}
d_{BL}	Thickness of the *layered bottom layer*
C_{corr}	Correction value of the phonon dispersion relation of the A_1 mode of chalcopyrite-type $CuInS_2$; $C_{\mathrm{corr}} = 20.18$ cm^{-1}
C_{Strain}	Strain-induced shift of the Raman spectrum
d_{nom}	Nominal thickness
$d_{\mathrm{penetration}}$	Penetration depth
d_{TL}	Thickness of the *well-crystallized top layer*
D^{Z}_{XY}	Diffusion coefficient of species Z in compound XY
$D_0{}^{Z}_{\mathrm{XY}}$	Frequency factor for diffusion of species Z in compound XY
e	Electron charge: $1.60217733 \cdot 10^{-19}$ C
$\mathbf{e}_{\mathrm{S}}$, $\mathbf{e}_{\mathrm{I}}$	Unit vectors of the polarization of scattered and incident light
$\boldsymbol{E}$	Electric field
$E_{\mathrm{A}}{}^{Z}_{\mathrm{XY}}$	Activation energy for diffusion of species Z in compound XY
E_{bin}	Binding energy
E_{CB}	Energy of the conduction band
E_{F}	Fermi energy
E_{gap}	Band gap energy
E_{kin}	Kinetic energy
E_{VB}	Energy of the valence band
f_{c}	Fractional conversion of an experimental variable ζ
F	Faraday constant: $9.6485309 \cdot 10^{4}$ C/mol
FF	Fill factor
f_{us}	Frequency of ultrasonic source
G	Free energy
H	Free enthalpy
$\underline{\boldsymbol{H}}$	Hamiltonian
h	Planck constant: $6.6260755 \cdot 10^{-34}$ Js
$\hbar$	$h/2\pi$
hkl	Miller indices
I_{CuAu}	Intensity of the A_1 mode of CuAu-ordered $CuInS_2$
$I_{\mathrm{D}} / I_{\mathrm{G}}$	Peak intensity ratio of the carbon Raman D- and G-modes
I_{I}	Intensity of incident light
I_{S}	Intensity of scattered light
I_0	Intensity factor of a Raman mode in the PCM formalism
$I(\omega)$	Spectral distribution of a Raman mode

J	Current density
$\boldsymbol{j}_{D}$	Particle current density
J_{photo}	Photo current density
J_{Pmax}	Current density at the maximum power point
J_{SC}	Short-circuit-current-density
j_1	First order spherical Bessel function
J_0	Saturation current density
k	Rate of a reaction of phase transformation
k_B	Boltzmann constant: $1.380658 \cdot 10^{-23}$ J/K
L	Correlation length
$L_{D_{XY}^{Z}}$	Diffusion length, as calculated form D_{XY}^{Z} using Eq. (4.11)
n_i	Amount of species i
n_p	Minority carrier density (electrons)
p	Pressure or strain
$\boldsymbol{P}$	Polarization
p_n	Minority carrier density (holes)
P	Power
P_{in}	Power of incident radiation
P_{max}	Maximum Power
P_{Laser}	Laser power
p_s	Saturated vapor pressure
$\boldsymbol{q}$	Wave vector in reciprocal space
$\boldsymbol{Q}$	Atomic displacement
QE_{max}	Maximum of a QE-curve
R_{I-III}, R_{II-III}	Distances between the group I, II and III atoms in the chalcopyrite lattice
R_{BZ}	Radius of an averaged Brillouin zone
$\boldsymbol{R}$	Radius of a spherical crystal
$\underline{\boldsymbol{R}}$	Raman Tensor
$\boldsymbol{r}$	Vector of a point in real space
r	Ratio: $p_s / (\sigma_{surf} \cdot \eta_{vis})$
R_{shunt}	Shunt resistance
R_{series}	Series resistance
R_{XY}	Distance between atoms X and Y
R^2	Coefficient of determination
S	Entropy
$S(\boldsymbol{q})$	Structure factor in PCM II
T	Temperature
t	Time
$T_{aerosol}$	Aerosol preheating temperature
$T_{decomposition}$	Decomposition temperature of a compound
$T_{sublimation}$	Sublimation temperature of a compound
T_{Sub}	Substrate temperature
U	Internal energy
V	Voltage
V'	Volume
V_{OC}	Open-circuit-voltage
V_{Pmax}	Voltage at the maximum power point
V_T	Thermal voltage
V_{XY}	Vacancy of element XY in a crystal lattice
x_Y	Relative molar amount of element Y

$X_{A_xB_y}$	Relative molar content of compound A_xB_y
$y_{A_xB_y}$	Relative molar amount of compound A_xB_y
z	Electric charge of a diffusing species
α_{abs}	Absorption coefficient
α_{Auger}	Auger parameter
α_{exp}	Thermal expansion coefficient
$\mathit{\Gamma}$	Natural line width of a Raman mode
Γ	Irreducible representation
$\mathit{\Delta}$	Difference
$\mathit{\Delta} t_X$	Duration of process X
Δ	Laplace Operator
ε_0	Electric field constant: $8.854 \cdot 10^{-12}$ F/m
η	Solar conversion efficiency
η_{vis}	Dynamic viscosity
η_{tet}, u	Tetragonal distortion parameters
κ	Extinction coefficient
λ	Wavelength
μ_i	Chemical potential of species i
ν	Photon frequency
ξ	Asymmetry factor of an asymmetric Lorentzian
ρ	Density
σ_{con}	Electrical conductivity
σ_{surf}	Surface tension
σ_{xy}	Standard deviation of parameter xy
φ	Electric potential
$\boldsymbol{\chi}$	Susceptibility tensor
ω, $\mathit{\Omega}$	Phonon frequencies
$\omega(\boldsymbol{q})$	Phonon dispersion relation
$\omega_{ave}(q)$	Averaged one-dimensional phonon dispersion relation
ω_{CuAu}	Peak center position of the A_1 mode of CuAu-ordered $CuInS_2$
$\mathit{\Phi}$	Photon flux of incident light
∇	Gradient
$\{hkl\}$	Lattice plane with Miller indices hkl
$[hkl]$	Lattice direction with Miller indices hkl
□	Vacancy in a sum formula of a compound
$\lvert a\rangle, \langle a\rvert$	Quantum mechanical states

IV Phase Diagrams

The Cu-S phase diagram

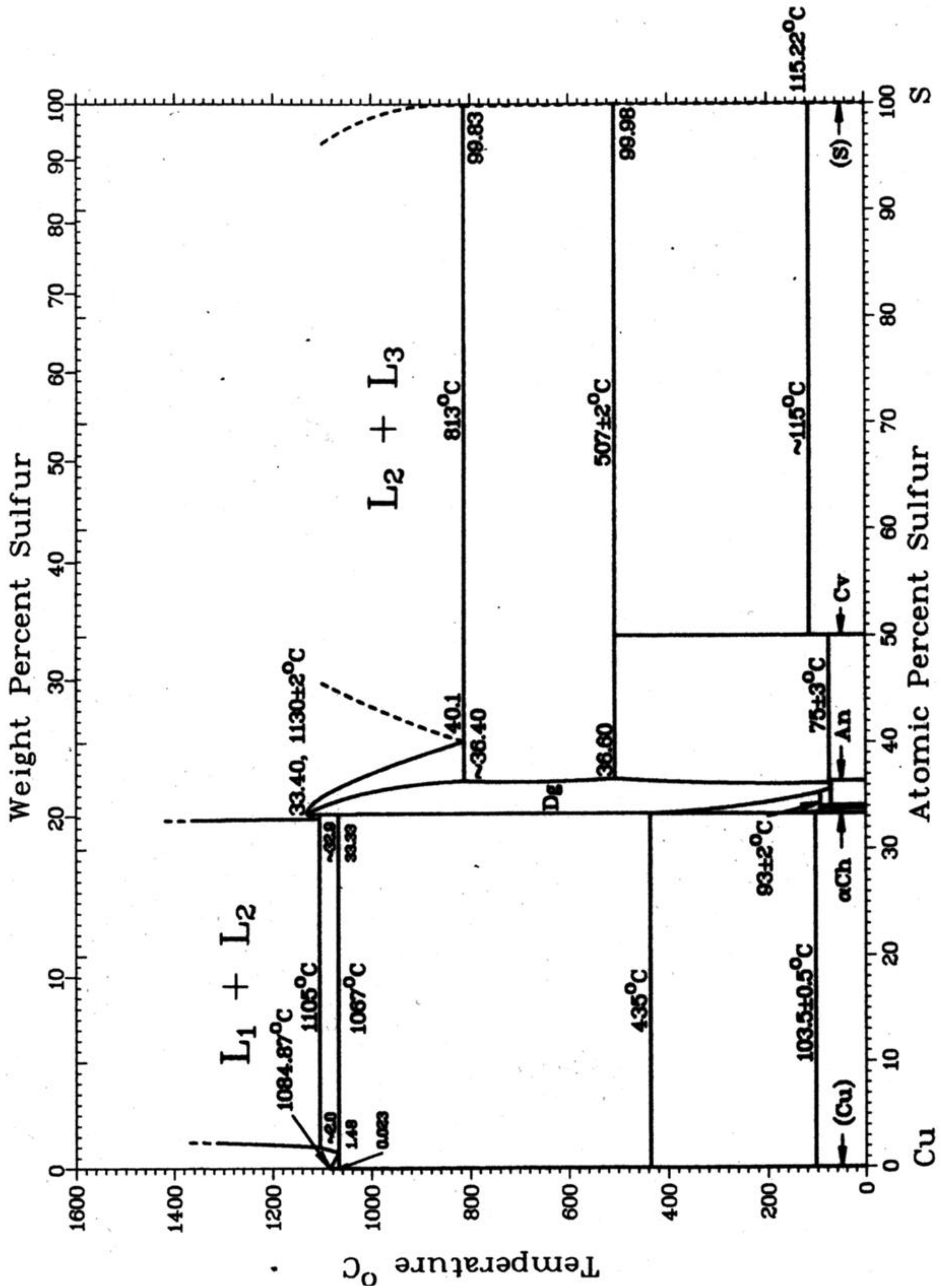

Fig. IV.1: The Cu-S phase diagram [Massalski '90]

The In-S phase diagram

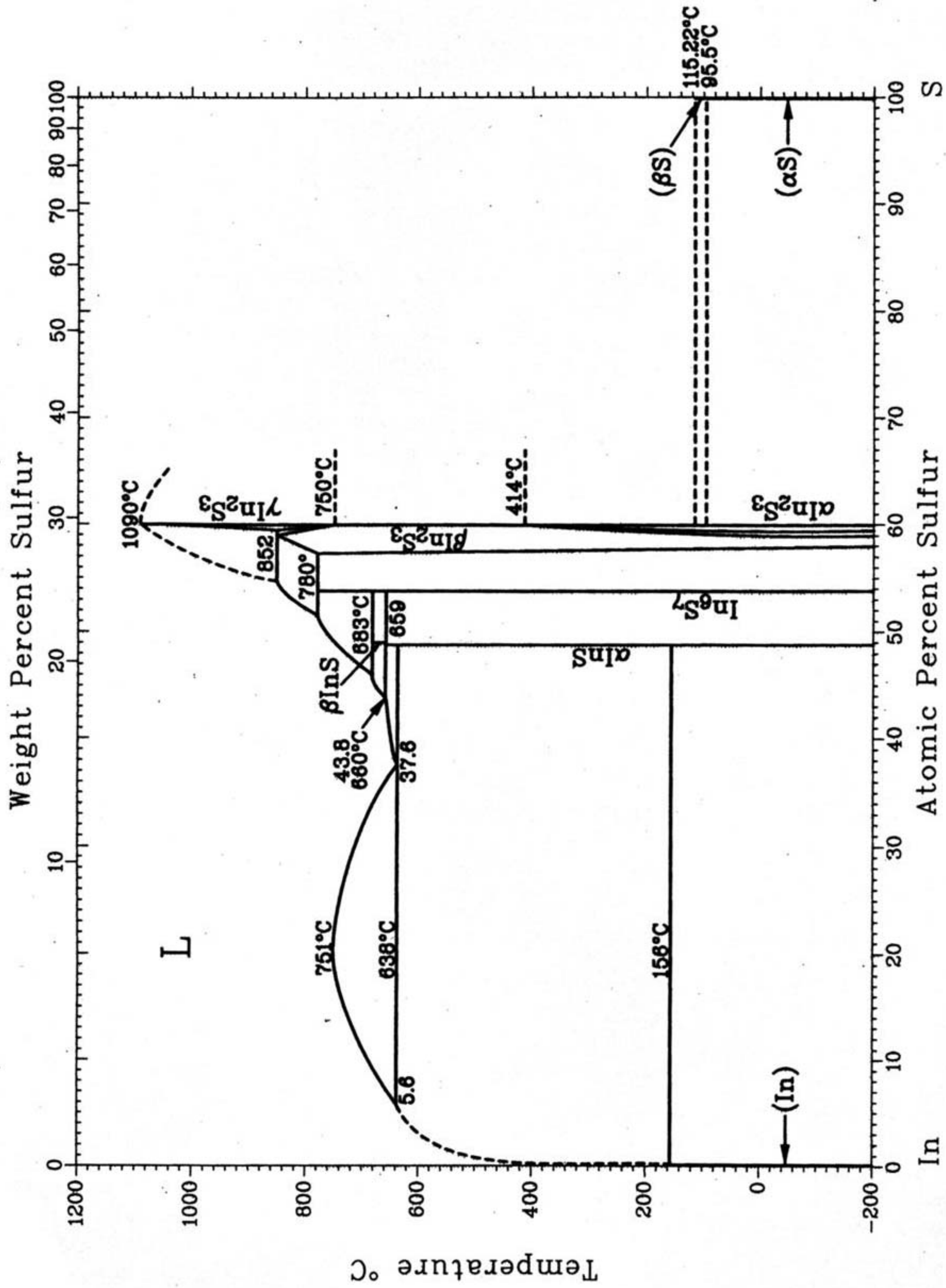

Fig. IV.2: The In-S phase diagram [Massalski '90]

V Diffusion Coefficients

Table V.1: Literature values for the frequency factors D_0, the diffusion coefficients D and the activation energies E_A of different diffusing species (copper, indium, sulfur, oxygen, selenium) in various polycrystalline (pc) and / or single-crystalline (sc) materials ($CuInS_2$; $CuInS_ySe_{1-y}$ with $0.3 \leq y \leq 1$; In_2S_3; $In_2Se_3/CuGaSe_2$; In_2O_3; β-Cu_2S; $Cu_{2-\delta}S$; CuS; Cu_2Se; tetrahedral amorphous (ta) carbon and graphite) as they were reported in the respective references. Bold values were directly taken from the references, whereas italic values were calculated from the values in the reference, according to Eq. (4.11). "n.r." stands for "not reported". T_{Lit} is the temperature stated in the references. Only those phases are listed, which are stable at or close to the growth or annealing temperatures of the Spray ILGAR $CuInS_2$ thin films of 430 °C and 550°C, respectively.

Diffusing species	**Material**	**D_0 [cm^2s^{-1}]**	**D (T_{Lit}) [cm^2s^{-1}]; T_{Lit} [°C]**	**E_A [eV]**	**Reference**	**D (430°C) [cm^2s^{-1}]**	**D (550°C) [cm^2s^{-1}]**
Ternary compounds							
Cu	pc-$CuInS_2$	n. r.	**$4.2\cdot10^{-9}$-$3.3\cdot10^{-7}$; 25**	n. r.	[Kleinfeld '88]	/	/
Cu	sc-$CuInS_2$	n. r.	**$2.3\cdot10^{-9}$-$3.2\cdot10^{-6}$; 25**	n. r.	[Kleinfeld '88]	/	/
In	pc-$CuInS_2$	n. r.	**$2.7\cdot10^{-10}$-$1.9\cdot10^{-8}$; 650**	n. r.	[Wissmann '97]	/	/
S	sc-$CuInS_ySe_{1-y}$ for $0.3 \leq y \leq 1$	n. r.	**$1.0\cdot10^{-16}$; 575**	n. r.	[Titus '06]	/	/
Binary indium compounds							
In	In_2S_3	n. r.	n. r.	n. r.	/	/	/
S	sc-In_2S_3	*134.23*	**$3.2\cdot10^{-7}$; 600**	**1.51**	[Tezlevan '93]	*$2.0\cdot10^{-9}$*	*$7.6\cdot10^{-8}$*
In	pc-In_2Se_3/ $CuGaSe_2$	**$8.1\cdot10^{-11}$**	**$3.3\cdot10^{-13}$; 400**	**0.32**	[Djessas '04]	*$4.0\cdot10^{-13}$*	*$8.9\cdot10^{-13}$*
In	In_2O_3	n. r.	n. r.	n. r.	/	/	/
O	pc-In_2O_3	**$5.24\cdot10^{7}$**	**$6.2\cdot10^{-17}$; 800**	**5.1**	[Ikuma '96]	*$1.7\cdot10^{-29}$*	*$3.6\cdot10^{-24}$*
O	sc-In_2O_3	**$7.4\cdot10^{5}$**	**800°C≤T_{Lit}≤1200°C**	**6.1**	[Ikuma '98]	*$1.4\cdot10^{-38}$*	*$3.2\cdot10^{-32}$*
Binary copper compounds							
Cu	pc-β-Cu_2S	**$2.06\cdot10^{-4}$**	**$2.4\cdot10^{-7}$; 150**	**0.25**	[Pauporte '99]	*$3.6\cdot10^{-5}$*	Not stable
Cu	pc blend of β-Cu_2S/$Cu_{2-\delta}S$	n. r.	**$2.0\cdot10^{-7}$; 150**	n. r.	[Pauporte '98]	/	/
Cu	pc blend of CuS/β-Cu_2S/ $Cu_{2-\delta}S$	**$8.76\cdot10^{-4}$**	**297°C≤T_{Lit}≤507°C**	**0.23**	[Bartkowicz '86]	*$2.0\cdot10^{-5}$*	*$3.4\cdot10^{-5}$*
	pc-β-Cu_2S		**507°C≤ T_{Lit} ≤1120°C**				
Cu	$Cu_{2-\delta}S$	*0.0163*	**$4.8\cdot10^{-8}$; 55**	**0.36**	[Price '81]	*$4.3\cdot10^{-5}$*	*$1.0\cdot10^{-4}$*
S	Cu_xS for $1 \leq x \leq 2$	n. r.	**$D^S \approx 10^5\cdot D^{Cu}$**	n. r.	[Blachnik '01]	/	/
In	Cu_2Se	n. r.	**$4.2\cdot10^{-6}$; 650**	n. r.	[Park '00]	/	/
Carbon modifications							
Cu	ta-carbon	/	**no diffusion for T<1000 °C**	/	[Kröger '03]	/	/
Ag	ta-carbon	/		/		/	/
Cu	graphite	/	**Diffusion only through defects**	/	[Jackson '95]	/	/
Ag	graphite	/		/		/	/

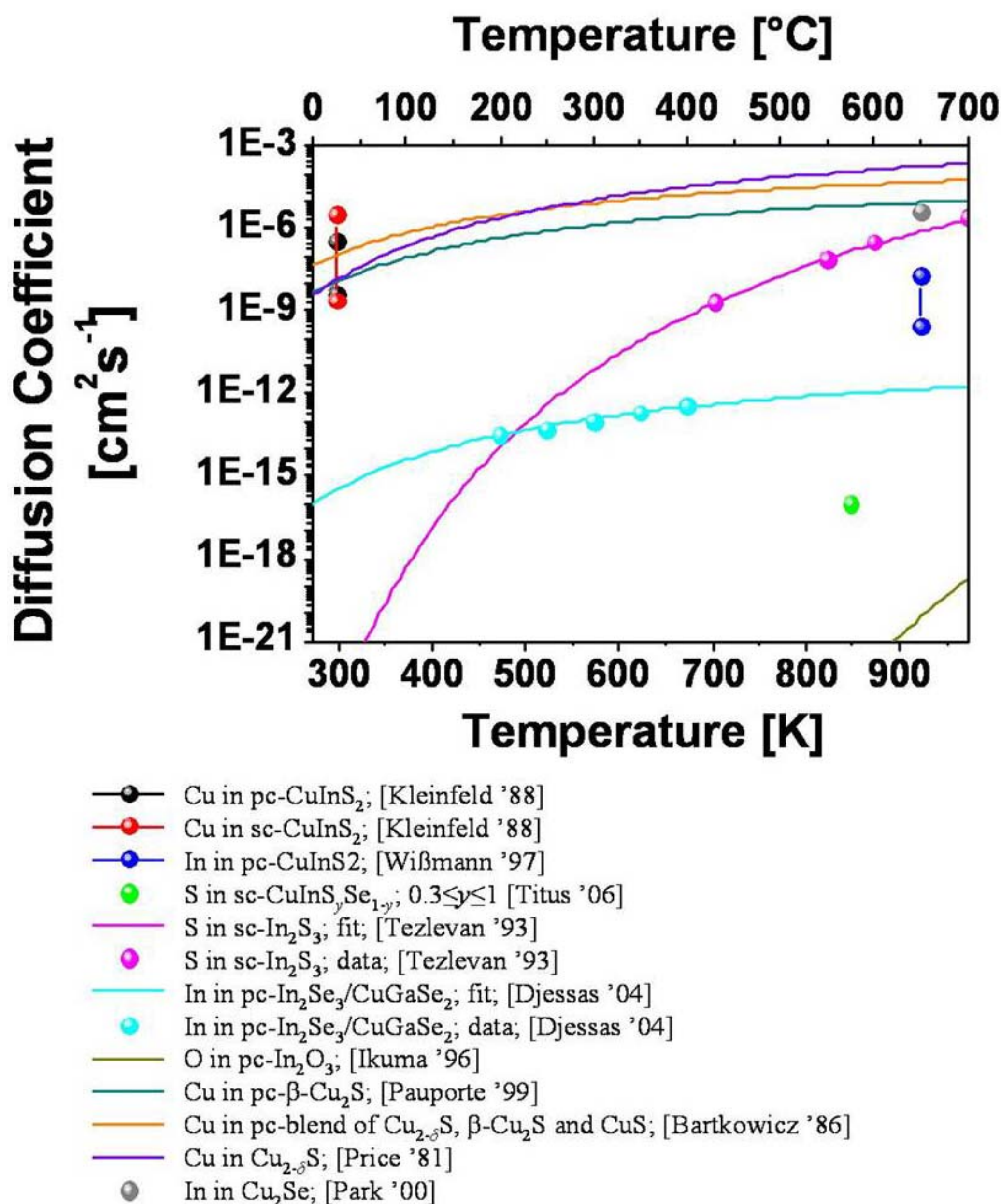

Fig. V.1: Literature data for the diffusion coefficients of different diffusing species (copper, indium, sulfur, oxygen, selenium) in various polycrystalline (pc) and / or single-crystalline (sc) materials ($CuInS_2$; $CuInS_ySe_{1-y}$ with $0.3 \leq y \leq 1$; In_2S_3; $In_2Se_3/CuGaSe_2$; In_2O_3; β-Cu_2S; $Cu_{2-\delta}S$; CuS and Cu_2Se) as they were reported in the respective references. The corresponding values for the frequency factors D_0, the diffusion coefficients D and the activation energies E_A are listed in Table V.1.

VI Mathcad Fitting Routine

Definition of $S(q) \cdot q^2$:

$$Bessel(x, CorrLength) := \frac{9 \cdot js(1, x \cdot CorrLength)^2}{CorrLength^2}$$

Read data from file:

Se305 :=

	0	1
0	320.371	8.559

$X := Se305^{\langle 0 \rangle}$

$Y := Se305^{\langle 1 \rangle}$

X =

	0
0	320.371
1	319.294

Y =

	0
0	8.559
1	-10.035

Fig. VI.1: Definition of the structure factor function (left) and upload of the data to be fitted (right)

Define function type to be fitted:
Write the function,

$$\left[\int_0^{0.089944234} \frac{P_1 \, Bessel(x \cdot \pi, P_0)}{\left[\omega - P_4 - 21.15797 - \left[\left[\left[\frac{8.10161 + 1.59351\frac{x}{0.512117892} + 8.36849\left(\frac{x}{0.512117892}\right)^2 - 569.72762\left(\frac{x}{0.512117892}\right)^3 + 4590.50093\left(\frac{x}{0.512117892}\right)^4 - 10018.74343\left(\frac{x}{0.512117892}\right)^5 + 8.65578 - 0.53995\cos\left(\frac{x}{0.359776936} \cdot \frac{3.14}{1}\right)^2 + 0.50504\frac{x}{0.359776936} + -0.24867\left(\frac{x}{0.359776936}\right)^2 + 8.11482}{3}\right.\right.\right.\right.}$$

$$\left.\left.\left.\left. \cdots 0.28459\frac{x}{0.40434172} + 42.4251\left(\frac{x}{0.40434172}\right)^2 - 524.20312\left(\frac{x}{0.40434172}\right)^3 + 2524.94607\left(\frac{x}{0.40434172}\right)^4 - 4204.00461\left(\frac{x}{0.40434172}\right)^5\right] \cdot 33.3564\right]\right]^2 + \frac{3.0433^2}{4} \, dx\right] + \frac{P_2}{1 + \left(\frac{\omega - 306.020277}{P_3}\right)^2}$$

Fig. VI.2: Definition of the PCM function, i.e. the function describing the spectral shape of the A_1 mode of chalcopyrite $CuInS_2$, in term of a vector, whose components are the unknown parameters, which follow from the fit. The red line indicates the line break. The denominator contains the corrected and averaged one-dimensional phonon dispersion relation of the A_1 mode of chalcopyrite-type $CuInS_2$ $\omega_{ave}(q)$ as it was obtained by fitting the data in Ref. [Lazewski '02] by superimposed power and cosine functions.

Define fitting parameters:

$$Pg := \begin{pmatrix} 10 \\ 10000000 \\ 600 \\ 4 \\ 1 \end{pmatrix}$$

Vector of guess values for unknown parameters

P0=Correlation length,
P1=Intensity,
P2=CuAu Intensity,
P3=CuAu-FWHM,
P4=Strain shift,
CuAu-Position has to be inserted manually

This is a vector-valued function whose first component is the function to be fitted and whose remaining components are the derivatives with respect to each parameter of tha function.

Definition CuAu-contribution and ist partial derivatives:

CuAu-Beitrag

$Lo0 := 180 \quad Lo1 := 303.3 \quad Lo2 := 3.25$

$$Lore(\omega) := \frac{Lo0}{1 + \left(\frac{\omega - Lo1}{Lo2}\right)^2}$$

$$\frac{d}{dP2} \frac{P2}{1 + \left(\frac{\omega - 306.020277}{P3}\right)^2} \rightarrow \frac{1}{1 + \frac{(\omega - 306.020277)^2}{P3^2}}$$

$$\frac{d}{dP3} \frac{P2}{1 + \left(\frac{\omega - 306.020277}{P3}\right)^2} \rightarrow 2 \cdot \frac{P2}{\left[1 + \frac{(\omega - 306.020277)^2}{P3^2}\right]^2} \cdot \frac{(\omega - 306.020277)^2}{P3^3}$$

Fig. VI.3: Guess values for the unknown parameters and definition of the partial derivatives. The Correlation length (P0) corresponds to the radius of the confining sphere and is given in units of Å. The intensities (P1, P2) are given in arbitrary units. The strain shift as well as the FWHM of the A_1 mode of CuAu-ordered $CuInS_2$ and its peak center position are given in units of cm^{-1}.

$$derP0Bessel(x, P0) := \frac{d}{dP0} Bessel(x, P0)$$

$$\frac{d}{dP4} \int_0^{0.089944234} \frac{P1 \cdot Bessel(x, P0)}{\left[\omega - P4 - 21.15797 - \left[\left[8.10161 + 1.59351 \frac{x}{0.512117892} + 8.36849 \left(\frac{x}{0.512117892}\right)^2 - 569.72762 \left(\frac{x}{0.512117892}\right)^3 + 4590.50093 \left(\frac{x}{0.512117892}\right)^4 - \ldots\right.\right.\right.}$$

$$\ldots 0018.74343 \left(\frac{x}{0.512117892}\right)^5 + 8.65578 - 0.53995 \cos\left(\frac{x}{0.359776936} \cdot \frac{3.14}{1}\right)^2 + 0.50504 \frac{x}{0.359776936} + -0.24867 \left(\frac{x}{0.359776936}\right)^2 + 8.11482 - 0.28459 \frac{x}{0.40434172} + 42.42\ldots$$

$$\ldots 3$$

$$\ldots \left(\frac{x}{0.40434172}\right)^2 - 524.20312 \left(\frac{x}{0.40434172}\right)^3 + 2524.94607 \left(\frac{x}{0.40434172}\right)^4 - 4204.00461 \left(\frac{x}{0.40434172}\right)^5 \Bigg] \cdot 33.3564 \Bigg]\Bigg]^2 + \frac{3.0433^2}{4} \Bigg] dx + \frac{P2}{1 + \left(\frac{\omega - 306.020277}{P3}\right)^2} \rightarrow \int_0^{\ldots}$$

9944234e-1

$-9 \cdot P1 \cdot \frac{js(1, \ldots}{P0^2 \cdot \left[\left(\omega - 1 \cdot P4 - 21.157970000000000001 \cdot |276.549128548000000000\ 42.379651726389388070 + 3218.6757961523064206^2 - 135332.6882077806 \ldots\right.\right.}$

P0)^2 ... $\cdot(-2 \cdot \omega + 2 \cdot P4 + \ldots$

22d^3 + 1792364.5055352387132^4 − 7487356.2019793537068^5 − 6.003596059999999999cos(8.7276300557521007960^2|)^2 + 2.31541872250000000000

2.31594000000000000 2 · |276.549128548000000000 42.379651726389388070 + 3218.6757961523064206^2 − 135332.6882077806422d^3 + 1792364.5055352387132^4 − 7…

Fig. VI.4: Partial derivative of the PCM function (Fig. VI.2) with respect to P4 (strain-induced shift). The red lines indicates the line break.

$$F(\omega,P) := \int_0^{0.089944234} \frac{P_1\,\text{Bessel}(x\,\pi,P_0)}{\left[\omega - P_4 - 21.15797 - \left[\left[\frac{8.10161 + 1.59351\frac{x}{0.512117892} + 8.36849\left(\frac{x}{0.512117892}\right)^2 - 569.72762\left(\frac{x}{0.512117892}\right)^3 + 4590.50093\left(\frac{x}{0.512117892}\right)^4 - 10018.74343\left(\frac{x}{0.512117892}\right)^5 + 8.65578 - 0.53995\cos\left(\frac{x}{0.359776936}\cdot\frac{3.14}{1}\right)^2 + 0.50504\frac{x}{0.359776936} + -0.24867 \ldots}{3}\right.\right.\right.}$$

$$\int_0^{0.089944234} \frac{P_1\,\text{derP0Bessel}(x\,\pi,P_0)}{\left[\omega - P_4 - 21.15797 - \left[\left[\frac{8.10161 + 1.59351\frac{x}{0.512117892} + 8.36849\left(\frac{x}{0.512117892}\right)^2 - 569.72762\left(\frac{x}{0.512117892}\right)^3 + 4590.50093\left(\frac{x}{0.512117892}\right)^4 - 10018.74343\left(\frac{x}{0.512117892}\right)^5 + 8.65578 - 0.53995\cos\left(\frac{x}{0.359776936}\cdot\frac{3.14}{1}\right)^2 + 0.50504\frac{x}{0.359776936} + -0. \ldots}{3}\right.\right.\right.}$$

$$\int_0^{0.089944234} \frac{\text{Bessel}(x\,\pi,P_0)}{\left[\omega - P_4 - 21.15797 - \left[\left[\frac{8.10161 + 1.59351\frac{x}{0.512117892} + 8.36849\left(\frac{x}{0.512117892}\right)^2 - 569.72762\left(\frac{x}{0.512117892}\right)^3 + 4590.50093\left(\frac{x}{0.512117892}\right)^4 - 10018.74343\left(\frac{x}{0.512117892}\right)^5 + 8.65578 - 0.53995\cos\left(\frac{x}{0.359776936}\cdot\frac{3.14}{1}\right)^2 + 0.50504\frac{x}{0.359776936} + -0. \ldots}{3}\right.\right.\right.}$$

$$\frac{1}{1 + \frac{(\omega - 306.02027)^2}{(P_3)^2}}$$

$$2\cdot\frac{P_2}{\left[1 + \frac{(\omega - 306.02027)^2}{(P_3)^2}\right]^2}\cdot\frac{(\omega - 306.02027)^2}{(P_3)^3}$$

$$\int_0^{.89944234e-1} -9\cdot P_1\cdot\frac{js(1.x\,\pi\,P_0)^2}{(P_0)^2\cdot\left[\left(\omega - 1\cdot P_4 - 21.157970000000000001\cdot\left|276.549128548000000042.379651726389388070 - 3218.6757961523064206 - 13533 \ldots .68820778064221 + 1792364.50553523871i2 - 7487356.20197935370i8 - 6.0035960599999999999\cos(8.727630055752100798x)\right|\right)^2 + 2.3154187225000000000\right]^2}\cdot\left(-2\cdot\omega + \ldots\right)$$

Fig. VI.5: First part of the fitting matrix. To be continued...

Fig. VI.6: Continuation of the fitting matrix. To be continued...

$$\overline{\ldots 76936}\Big)^2 + 8.11482 - 0.28459\frac{x}{0.40434172} + 42.4251\left(\frac{x}{0.40434172}\right)^2 - 524.20312\left(\frac{x}{0.40434172}\right)^3 + 2524.94607\left(\frac{x}{0.40434172}\right)^4 - 4204.00461\left(\frac{x}{0.40434172}\right)^5\Bigg]\cdot 33.3564\Bigg|\Bigg|^2 + \frac{3.0\ldots}{\ldots}$$

$$\ldots 4867\left(\frac{x}{0.359776936}\right)^2 + 8.11482 - 0.28459\frac{x}{0.40434172} + 42.4251\left(\frac{x}{0.40434172}\right)^2 - 524.20312\left(\frac{x}{0.40434172}\right)^3 + 2524.94607\left(\frac{x}{0.40434172}\right)^4 - 4204.00461\left(\frac{x}{0.40434172}\right)^5\Bigg]\cdot 33.3\ldots$$

$$\ldots 4867\left(\frac{x}{0.359776936}\right)^2 + 8.11482 - 0.28459\frac{x}{0.40434172} + 42.4251\left(\frac{x}{0.40434172}\right)^2 - 524.20312\left(\frac{x}{0.40434172}\right)^3 + 2524.94607\left(\frac{x}{0.40434172}\right)^4 - 4204.00461\left(\frac{x}{0.40434172}\right)^5\Bigg]\cdot 33.3\ldots$$

$$\ldots 2\cdot P_4 + 42.315940000000000002\cdot\Big|276.549128548000000042.37965172638938880 - 3218.6757961523064256^2 - 135332.6882077806421^3 + 1792364.505535238712^4 \ldots$$

Fig. VI.7: Continuation of the fitting matrix. To be continued...

$$\ldots\, dx\Bigg] + \frac{P_2}{1 + \left(\frac{\omega - 306.02027}{P_3}\right)^2}$$

$$\ldots 3^2$$

$$\ldots\, dx\Bigg]$$

$$\ldots 64\Big|\Big|^2 + \frac{3.0433^2}{4}$$

$$\ldots\, dx$$

$$\ldots 64\Big|\Big|^2 + \frac{3.0433^2}{4}$$

$$\ldots 7487356.2019793537068^5 - 6.0035960599999999996\cdot(8.72763005575210079\omega^2\Big|\Big)\, dx$$

Fig. VI.8: Continuation of the fitting matrix.

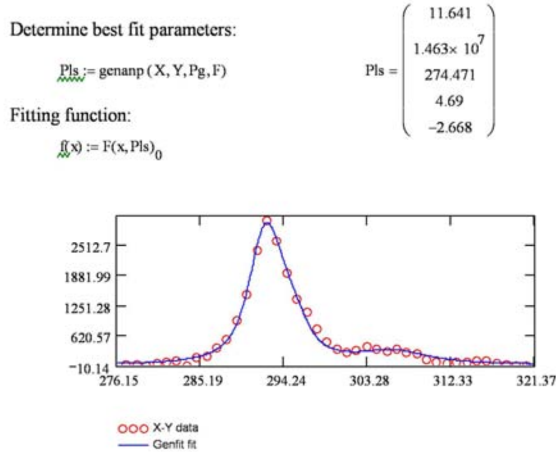

Fig. VI.9: Parameters resulting from the fit and resulting spectral shape of the A_1 mode (blue trace). The red circles represent the measured data.

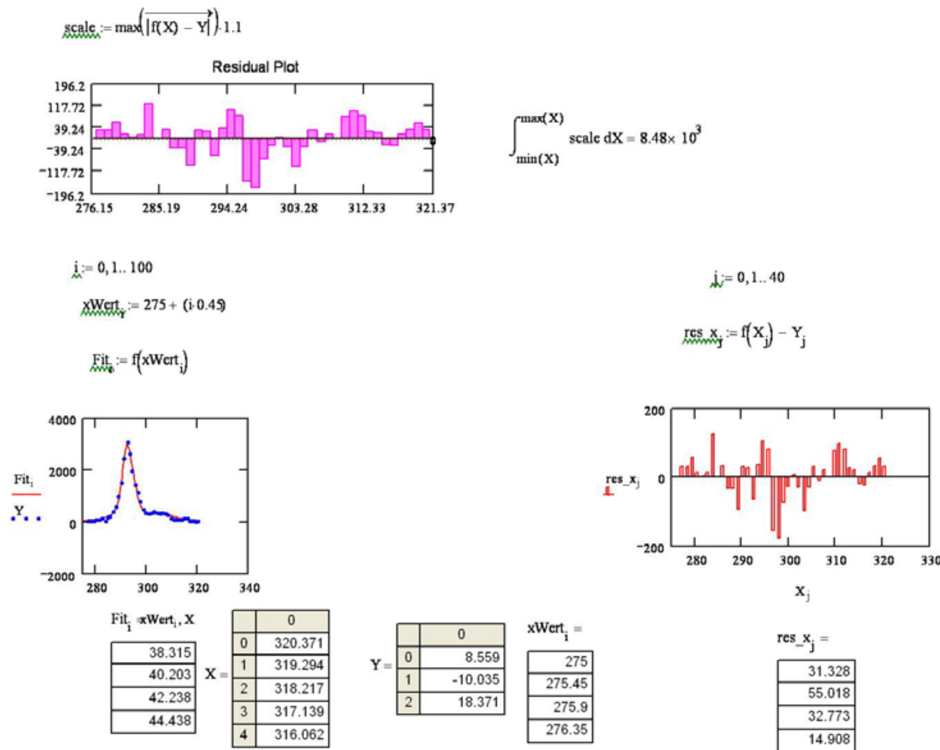

Fig. VI.10: Residuals of the fit and parameterization of the fits in order to export it.

The goodness of the approximation of measured Raman spectra with simulated spectra was assessed by calculating the *coefficient of determination* R^2 of the fits. The definition of R^2 is given in Eq. (VI.1).

$$R^2 \equiv 1 - \frac{\sum_i \left(I_i^{\text{measured}} - I_i^{\text{simulated}}\right)^2}{\sum_i \left(I_i^{\text{measured}} - \left\langle I^{\text{average}}\right\rangle\right)^2} \qquad \text{Eq. (VI.1)}$$

Here, I_i^{measured} is the *i*-th intensity value of the measured Raman spectrum, whilst $I_i^{\text{simulated}}$ is the *i*-th intensity value of the simulated Raman spectrum. $\langle I^{\text{average}}\rangle$ is the average intensity value of the measured Raman spectrum. For a simulated spectrum, which perfecly matches the measured spectrum, R^2 equals 1.

VII Analysis Techniques

In this section, a brief review of the characterization methods, which were used for the characterization of the thin films in the course of this thesis, is given. This review is restricted to the fundamental mechanism underlying the respective methods and to the main experimental parameters used for the measurements. Additionally, if applicable, the uncertainty or resolution of the methods is shortly discussed. For detailed discussions about the analysis techniques, the reader is referred to the corresponding references in each subsection. A general overview of these techniques is given in Ref. [Durose '04].

VII.i X-ray Photoelectron (XPS) and Auger Spectroscopy (XAS)

XPS and XAS measurements are based on the photoelectric effect, which was firstly observed by Hertz in 1887 and described by Einstein in 1905 [Hertz '87; Einstein '05]. The principle of the photoelectric effect is depicted in Fig. VII.1a. In this effect a photon of energy $h\nu_1$ impinging on a solid surface, can remove an core level electron from the solid, if the photon energy exceeds the sum of the binding energy E_{bin} of the electron and of the work function Φ of the surface. The work function Φ is a constant of a given material and constitutes the difference between the Fermi-level E_F and the vacuum energy level E_{Vac}. After leaving the solid, the electron (Photoelectron) has a kinetic energy E_{kin} of:

$$E_{kin} = h\nu - E_{bin} - \Phi \quad \text{with} \quad \Phi = E_{Vac} - E_F \qquad \text{Eq. (VII.1)}$$

After the electron has been removed from the solid, an electron vacancy remains on its original energy level E_{bin_1}. This electron vacancy can be filled by another electron stemming from a higher energy level E_{bin_2}. The energy difference between E_{bin_1} and E_{bin_2} is set free as a photon. This photon can either be emitted by the solid (X-ray fluorescence, section VII.iii) or can remove an electron from another higher energy level E_{bin_3}, which then leaves the solid (Auger process; Fig. VII.1b). These electrons are referred to as Auger electrons and have a kinetic energy E_{kin} of:

$$E_{kin} = E_{bin_1} - E_{bin_2} - E_{bin_3} - \Phi \qquad \text{Eq. (VII.2)}$$

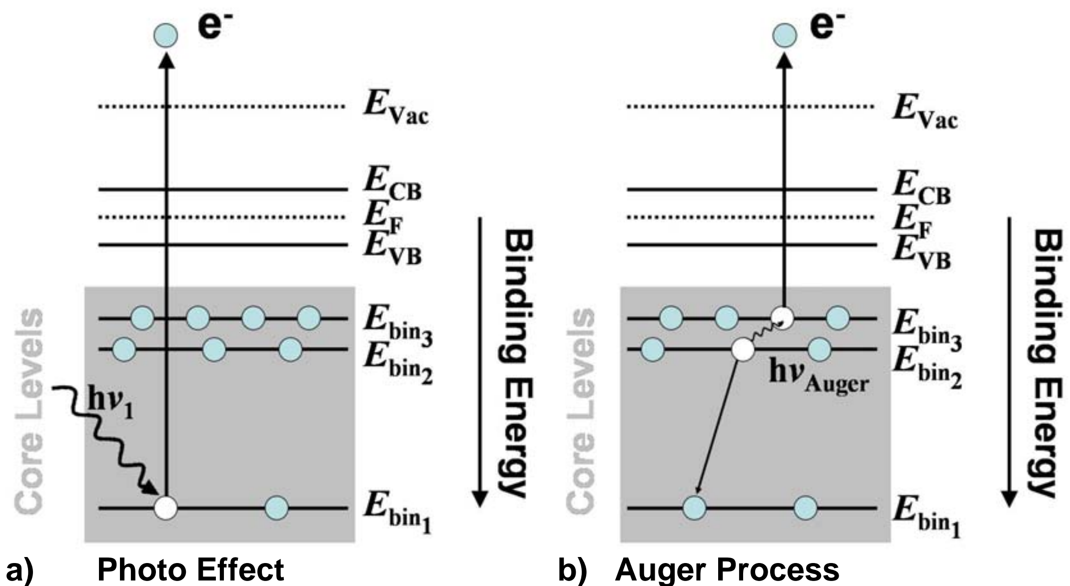

Fig. VII.1: Schematic sketch of the photoelectric effect (a) and of the subsequent Auger process (b), which are the physical basis for XPS and XAS measurements. Alternatively, the process of X-ray fluorescence can proceed instead of the Auger process (section VII.iii). The turquoise circles depict occupied electron states, whilst the white circles correspond to unoccupied states.

In XPS or XAS experiments, the photoelectrons or Auger electrons are detected, respectively. Their kinetic energy includes the information about the binding energy of the respective electrons (Eq. VII.1-2). These binding energies mainly depend on the element, from which the electron was expelled, but are also modified by the chemical bond of the respective atom. Therefore, XPS and XAS do not only provide information about the elemental composition of a surface but also about the compounds, in which the atoms are bound. These compounds can either be identified by referring to tabled values [Moulder '92] or by directly measuring reference materials. A more detailed description about XPS and XAS measurements can be found in Ref. [Moulder '92; Yu '05] and the references therein.
For the XPS-measurements of this thesis, an Al K_α source (hν = 1486.6 eV) and a CLAM4 electron spectrometer (Thermo VG Scientific) were used for excitation and for detection of the photo- and Auger electrons, respectively. Both are integrated in the CISSY-UHV-facility, which is described in Ref. [Reichardt '05]. For Al K_α excitation and the kinetic energies investigated in this thesis, the information depth of the XPS and XAS measurements is in the range of 0.1-10 nm [Moulder '92]. The smallness of the information depth is due to the smaller mean free path (0.1-10 nm) of the expelled electrons in a solid compared to photons (some 100 nm).
In all measurements, the Au4f spectrum of an UHV-stored Au-foil was measured as a reference for the detected energies. The energetic resolution of the XPS and XAS measurements of this thesis was ± 0.1 eV. All XPS-samples were exposed to ambient air for about 10 min after deposition. Afterwards, they were stored in nitrogen and sealed in polyethylene foil under nitrogen atmosphere for further sample transfer.

VII.ii X-ray Diffraction (XRD)

The interatomic distances in a solid are of the order of 0.1-1 nm. Therefore, X-rays with wavelengths, which are smaller or of the same order as these distances, are diffracted by the atoms in the solid. If the atoms in the solid are ordered, i.e. the solid is a crystal, monochromatic X-rays impinging on the crystal, will interfere with each other and produce an interference pattern, which is referred to as a X-ray diffractogram. The condition for constructive interference was described equivalently by Laue [Laue '13] and Bragg [Bragg '13]. According to Bragg, the impinging X-rays interfere constructively, if:

$$n \cdot \lambda = 2d_{hkl} \cdot \sin\Theta \qquad \text{Eq. (VII.3)}$$

Here, n is a natural number, λ is the X-ray wavelength, and d_{hkl} is the distance between to lattice planes. The angle Θ is the incidence and excidence angle of the X-ray. In Fig. VII.2, the deduction of Eq. (VII.3) is shown schematically.

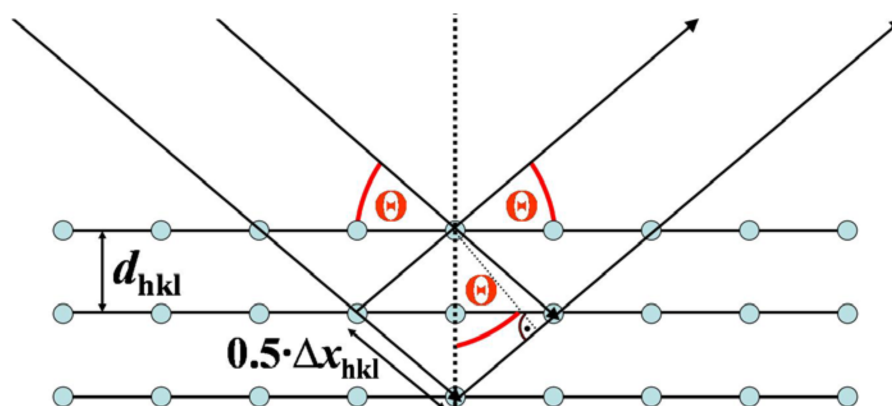

Fig. VII.2: Diffraction of impinging X-rays by the lattice planes of a crystal. The diffraction yields constructive interference, if the path difference Δx_{hkl} equals λ, which is expressed in Eq. (VII.3).

From these considerations, it becomes clear that X-ray diffractograms can only be obtained from solid, whose lattice exhibits a certain degree of crystalline order, whereas for amorphous solids, the diffractogram only consist of a single broad background peak. Usually an ordered array of more than 100 lattice planes are needed in order to obtain a diffractogram [Kittel '99]. A general introduction to X-ray diffraction is given in Ref. [Kittel '99] and the references therein.
In this thesis, X-ray diffraction was used for the identification of the crystalline phases in polycrystalline thin films. Therefore, the recorded X-ray diffractograms were compared to reference diffractograms to the data base of the Joint Committee on Diffraction Standards (JCPDS).
All XRD-measurements were performed in a Bruker D8 diffractometer in grazing incidence mode using a $CuK_{\alpha_{1,2}}$-source ($\lambda_{1,2}$ = 0.15406 nm / 0.15444 nm). Due to the limited thickness of the investigated films (<2 µm), all X-ray diffractograms, which were obtained in the course of this thesis, were recorded in grazing incidence mode using incidence angles α of 0.5 °-2 °, which corresponds to information depths of 0.5-2 µm for $CuInS_2$ [Neisser_2 '01]. In grazing incidence mode, the X-ray source is fixed and the X-rays impinge on the sample under a flat angle, whilst the detector is moved during the measurements. The detector angle β covered a range of 10 °-80 ° in the measurements. Here, the angle Θ in Fig. VII.2 equals $0.5\cdot(\alpha+\beta)$.

VII.iii X-ray Fluorescence (XRF) and Energy Dispersive X-ray Spectroscopy (EDX)

A general introduction to X-ray fluorescence measurements is given in Ref. [Williams '87].

X-ray Fluorescence (XRF)

As mentioned in section VII.i, the process of X-ray fluorescence occurs as a consequence of the photoelectric effect (Fig. VII.1a). After an electron has been removed from a core level E_{bin_1} by an incident X-ray, the electron vacancy can be filled by an electron stemming from a higher energy level E_{bin_2}. In case of X-ray fluorescence, the energy difference is emitted in form of a characteristic X-ray photon of energy $h\nu = E_{\mathrm{bin}_2} - E_{\mathrm{bin}_1}$ (Fig. VII.3).

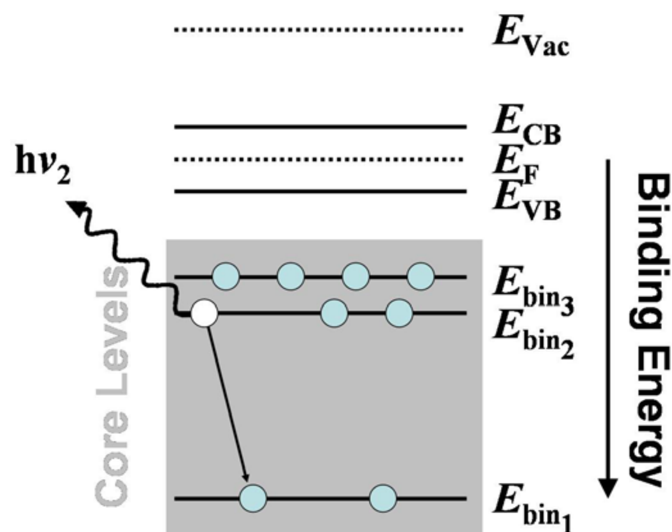

Fig. VII.3: Schematic sketch of the process of X-ray fluorescence, which can occur upon removal of a core electron by an impinging X-ray photon or an electron beam (photoelectric effect; Fig. VII.1a) alternatively to the Auger process (Fig. VII.1b). The turquoise circles depict occupied electron states, whilst the white circles correspond to unoccupied states.

In the XRF measurements that were performed in the course of this thesis, the probed sample is excited with X-rays emitted from a Rhodium anode. The X-rays are absorbed by the sample. Their absorption can be described as:

$$I(d) = I_0\cdot\exp(-\mu_m\cdot\rho\cdot d) \qquad \text{Eq. (VII.3)}$$

Here, $I(d)$ is the X-ray intensity in depth d in the sample, I_0 the initial intensity, whilst μ_m and ρ are the mass-absorption coefficient and the density of the absorbing material, respectively. If the probed sample consists of a compound, it mass-absorption coefficient can be calculated as the weighted sum of the different elements in the compound. Upon absorption of the impinging X-ray by the sample, photons of the characteristic X-ray lines of the elements in the sample are emitted. In first approximation, the intensity of the characteristic X-ray radiation emitted from the sample is proportional to the concentration of the elements. Therefore, the composition of the sample can be estimated by comparing the intensity to the intensity, which is emitted from reference elemental standards. However, a more precise way of determining the sample composition, is to calibrate the spectrometer with reference samples of the same compounds that are investigated. Furthermore, interactions between the elements in the sample and the impinging and emitted X-ray radiation have to be taken into account. In particular, reabsorption effects, i.e. the absorption of X-rays, which have been emitted by element A, by element B in a compound $A_\alpha B_\beta$, have to be considered.
In this thesis, the latter approach was followed by iteratively fitting the measured X-ray intensity using the Super Q software provided by Philips, which also determined the film thickness assuming bulk density. Two different calibration routines were prepared in the course of this thesis, which served for the determination of the thickness and of the [Cu]:[S] ratio in $Cu_{2-x}S$ ($0 \leq x \leq 0.2$) thin films and of the [Cu]:[In]:[S] ratio in $CuInS_2$ thin films.

The Cu_2S Calibration Routine

For the $Cu_{2-x}S$ calibration, a $Cu_{2-x}S$ thin film was prepared on a molybdenum-coated glass substrate by the Spray ILGAR method and its composition and thickness were determined by ERDA assuming the bulk density of 5.6 g/cm^3 of α-Cu_2S [www_4 '08]. By ERDA, the [Cu]:[S] ratio and the thickness of this film were determined as 0.48 ± 0.02 and 100 ± 15 nm, respectively. This sample was used to calibrate the intensities of the CuL_α and SK_α X-ray lines. Additionally, the intensity of the MoK_α X-ray line was included in the calibration, in order to take reabsorption effects into account. This calibration fitted the measured CuL_α, SK_α and MoK_α intensities assuming a molybdenum/$Cu_{2-x}S$ bilayer.

The $CuInS_2$ Calibration Routine

For the $CuInS_2$ calibration, the use of just one calibration sample was not sufficient. This was due to the fact, that the thicknesses of the investigated $CuInS_2$ thin films varied over a larger range compared to the $Cu_{2-x}S$ thin films. Therefore, the calibration was prepared using two different $CuInS_2$ thin films. The first one was a KCN etched RTP-$CuInS_2$ thin film, whose composition and thickness were determined as 24 ± 1 at. % Cu, 26 ± 1 at. % In and 50 ± 1 at. % S and 2070 ± 310 nm (by assuming a bulk density of 4.74 g/cm^3 [www_4 '08]) by ERDA. The second film was a KCN and H_2S treated Spray ILGAR $CuInS_2$ thin film with a composition of 23 ± 1 at. % Cu, 24 ± 1 at. % In and 52 ± 1 at. % S and a thickness of 603 ± 90 nm as determined by ERDA. These samples were used to calibrate the intensities of the CuK_α, CuL_α, InK_α, InL_α, SK_α and SK_β. The inclusion of the additional K- and L lines allowed for a higher reliability of the fits, which was found to be necessary in ternary samples. Additionally, the intensity of the MoK_α X-ray line was included in the calibration. This calibration fitted the measured CuK_α, CuL_α, InK_α, InL_α, SK_α, SK_β and MoK_α intensities assuming a molybdenum/$CuInS_2$ bilayer.

All XRF-measurements were performed in a Philips MagiX Pro wavelength-dispersive XRF spectrometer equipped with LiF-, Ge- and gas detectors. The uncertainties of the XRF-measurements have been determined by Rega as ± 0.5 at. % [Rega '04]. This is smaller than

the uncertainty of the composition determined by ERDA of ± 1 at. %. Hence the uncertainty of the XRF-determined composition is also ± 1 at. %. The same is true for the thickness [Wess '08], for which the uncertainty of the thickness is mainly due to deviations of the density from the bulk densities of 5.6 g/cm^3 for α-Cu_2S and of 4.74 g/cm^3 for $CuInS_2$ [www_4 '08] and is estimated as ± 15 % (relative) [Bohne '08].

Energy Dispersive X-ray Spectroscopy (EDX)

EDX measurements are also based on the effect of X-ray fluorescence, the main difference being, that the X-rays are not excited by incident X-rays, but by an electron beam with electron energies of 5-20 keV. These high-energetic electrons expel electrons from the core levels, so that characteristic X-rays can be emitted as it was described above (Fig. VII.3). Another difference to XRF is that emitted X-rays are detected by an EDX-detector, whose signal is proportional to the energy of the X-ray. This causes an energetic resolution, which is about 1-2 orders below that of wavelength-dispersive XRF measurements [Rega '04]. However, the advantage of EDX is that is coupled with a scanning electron microscope (section VII.iv), and therefore allows to measure the sample composition with a high spatial resolution of about 100 nm. Therefore, EDX was only used for qualitatively mapping the lateral changes in elemental composition, whereas XRF was used to measure the integral sample composition and thickness quantitatively.

VII.iv Scanning and Transmission Electron Microscopy (SEM, TEM)

By exciting a sample with an electron beam, highly resolved images of the sample can be obtained. The wavelength of the exciting electrons is the de Broglie wavelength, which follows from the beam energy and is usually in the range of some Ångströms. The lateral resolution is, however, determined by the electromagnetic lenses in the microscope and by the sample volume, which is excited by the electrons [Williams '87].
In SEM measurements, either the cross-section or the surface of a sample is excited by an electron beam with electron energies of about 10 keV. This beam is scanned over the sample and thereby excites the sample. Either the backscattered or secondary electrons are detected. Their intensity distribution reflects the surface morphology.
In TEM measurements, thin specimens are analogously analyzed by detecting electrons, which transmitted the specimen. Therefore, acceleration voltages of about 200 keV are applied. Due to the strong interaction between the electrons and the sample matrix, the specimen must not exceed a thickness of 100-200 nm. Therefore, a special preparation of the specimen is needed: Two thin film samples are glued together with conducting epoxy in face-to-face configuration [Bravman '84]. Afterwards, the samples are grinded to a thickness of about 30 µm. Finally, the thickness is reduced by ion-etching with 4 keV Ar^+-ions. In TEM measurements an atomic spatial resolution can be achieved. A brief introduction in electron microscopy and the corresponding sample preparation is given in Ref. [Durose '04].
For the SEM and EDX measurements a combined LEO1530 Gemini scanning electron microscope equipped with a Thermo Noran EDX detector was used. All measurements were performed with an acceleration voltage of 10 kV. The TEM images were acquired in a Zeiss LIBRA 200 transmission electron microscope equipped with an energy filter and a Thermo Noran EDX detector. The measurements have been performed by Dr. Daniel Abou-Ras and Ulrike Bloeck, who also prepared the TEM samples.

VII.v Elastic Recoil Detection Analysis (ERDA)

In ERDA-measurements high-energetic heavy ions (350 MeV Au ions) are elastically scattered at the sample atoms and the recoiling sample ions are detected [Bohne '98]. As the

ions enter the sample matrix, their energy decreases with depth due to the interaction with the sample. If the ion collides with a sample atom a certain amount of energy is transferred on the sample atom, which then is expelled from the sample. In ERDA measurements, the time of flight and the energy of the expelled sample atoms are simultaneously measured. From these data, the depth-dependent composition of the sample can be determined with an absolute error of ± 1 at. %. The depth-resolution of the composition is strongly affected by the surface roughness of the films and lies in the range of 10-70 nm. By assuming the bulk density of a material, also the thickness of the sample can be calculated, with an estimated relative error of ± 15 %. The major advantage of the ERDA method is that it does not require any standards and can detect all atoms, including light ones, such as hydrogen. Therefore, ERDA measurements can be used to obtain calibration standards for other methods, such as XRF. All ERDA measurements of this thesis have been performed by Dr. Wolfgang Bohne, Dr. Jörg Röhrich and Dr. Erik Strub in the ion beam lab (ISL) of the Hahn-Meitner-Institut Berlin. The ERDA method and the corresponding setup are described in detail in Ref. [Lindner '03; Bohne '08].

IIX Input Parameter for *QE*-Simulations

For the *QE*-Simulations, the program SCAPS was used, which was developed by Burgelman *et al.* and is described in Ref. [Burgelman '00; Burgelman '04]. The following parameters have been chosen on the basis of the values given in Ref. [Klenk '01] for $CuInS_2$ thin films.

Table IIX.1: Input parameters for the simulations of the *QE*-curves in Fig. 6.8 using the SCAPS software [Burgelman '00; Burgelman '04].

a) LAYER PROPERTIES				
Layer	**Defect-rich $CuInS_2$ (*bottom layer*)**	**Defect-poor $CuInS_2$ (*top layer*)**	**CdS**	**ZnO**
Thickness *d* [µm]	1.9; 1.8; 1.7; 1.6; 1.5; 1.4; 1.3; 1.2; 1.1; 1.0; 0.8; 0.6; 0.4; 0.2; 0.1	0.1; 0.2; 0.4; 0.6; 0.8; 1.0; 1.1; 1.2; 1.3; 1.4; 1.5; 1.6; 1.7; 1.8; 1.9	0.05	1
Bandgap E_{gap} [eV]	1.47 eV	1.47	2.42	3.30
Electron affinity [eV]	4.50	4.50	4.70	4.90
Dielectric permittivity (relative)	10	10	10	10
Effective density of states in conduction band [m^{-3}]	$1 \cdot 10^{25}$	$1 \cdot 10^{25}$	$1 \cdot 10^{25}$	$1 \cdot 10^{25}$
Effective density of states in valence band [m^{-3}]	$1 \cdot 10^{25}$	$1 \cdot 10^{25}$	$1 \cdot 10^{25}$	$1 \cdot 10^{25}$
Electron thermal velocity [m/s]	$1 \cdot 10^{5}$	$1 \cdot 10^{5}$	$1 \cdot 10^{5}$	$1 \cdot 10^{5}$
Hole thermal velocity [m/s]	$1 \cdot 10^{5}$	$1 \cdot 10^{5}$	$1 \cdot 10^{5}$	$1 \cdot 10^{5}$
Electron mobility [m^2/Vs]	$1 \cdot 10^{-4}$	$1 \cdot 10^{-4}$	$1 \cdot 10^{-4}$	$5 \cdot 10^{-4}$
Hole mobility [m^2/Vs]	$1 \cdot 10^{-4}$	$1 \cdot 10^{-4}$	$1 \cdot 10^{-4}$	$1 \cdot 10^{-4}$
Shallow donor density [m^{-3}]	0	0	$1 \cdot 10^{20}$	$1 \cdot 10^{24}$
Shallow acceptor density [m^{-3}]	$5 \cdot 10^{22}$	$5 \cdot 10^{22}$	0	0

b) DEFECT PROPERTIES							
Layer	**Defect-rich $CuInS_2$ (*bottom layer*)**	**Interface**	**Defect-poor $CuInS_2$ (*top layer*)**	**Interface**	**CdS**	**Interface**	**ZnO**
Type	Neutral	Neutral	Neutral	1) Donor; 2) Neutral	Neutral	Neutral	Neutral
Electron capture cross section [m^2]	$1 \cdot 10^{-19}$	$1 \cdot 10^{-19}$	$1 \cdot 10^{-19}$	1) $1 \cdot 10^{-19}$ 2) $1 \cdot 10^{-19}$	$1 \cdot 10^{-19}$	$1 \cdot 10^{-19}$	$1 \cdot 10^{-19}$
Hole capture cross section [m^2]	$1 \cdot 10^{-19}$	$1 \cdot 10^{-19}$	$1 \cdot 10^{-19}$	1) $1 \cdot 10^{-19}$ 2) $1 \cdot 10^{-19}$	$1 \cdot 10^{-19}$	$1 \cdot 10^{-19}$	$1 \cdot 10^{-19}$
Energy distribution	Single	Single	Single	1) Single 2) Single	Single	Single	Single
Energy level (from top of valence band) [eV]	0.75	0.75	0.75	1) 1.1 2) 0.75	1.21	1.21	1.65
Concentration [m^{-3}]	$1 \cdot 10^{23}$	$1 \cdot 10^{19}$	$1 \cdot 10^{21}$	1) $1 \cdot 10^{18}$ 2) $1 \cdot 10^{19}$	$1 \cdot 10^{22}$	$1 \cdot 10^{19}$	$1 \cdot 10^{22}$

IX AM 1.5 Solar spectrum

For terrestrial applications of solar cells the spectral composition of the sunlight is usually approximated by the standardized air mass 1.5 (AM 1.5) solar spectrum [NREL '08]. This spectrum describes the spectrum of the incident sunlight under an angle of 45 ° and takes the intensity losses, which are due to absorption processes in the atmosphere, into account. The standard conditions for *JV*-measurements under AM 1.5 illumination are T = 25 °C and an power density of the incident light of 100 mW/cm^2.

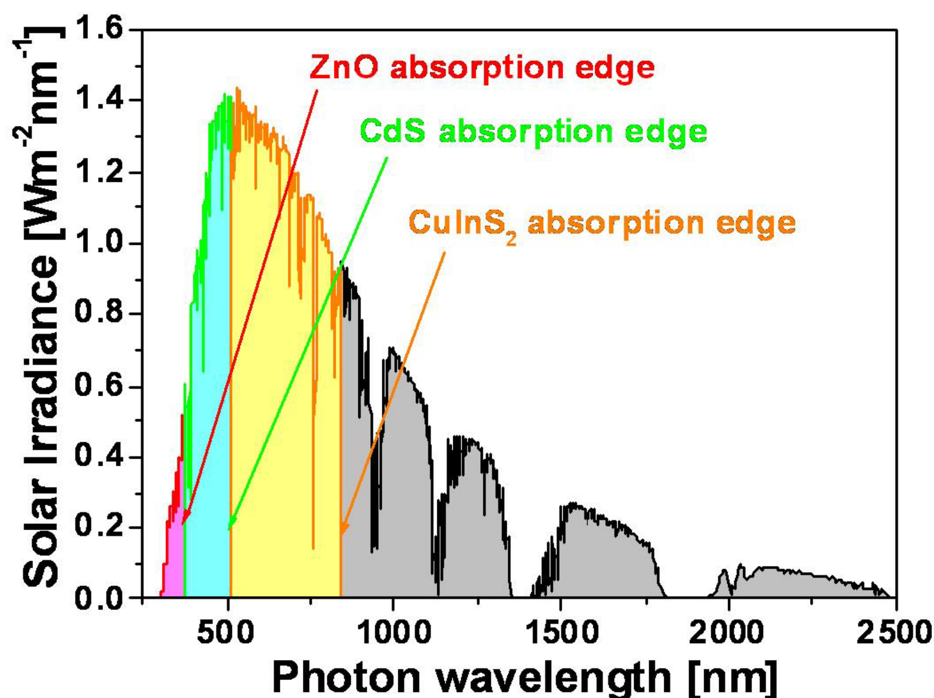

Fig. IX.1: Terrestrial solar spectrum AM 1.5. The red, green and yellow shaded areas mark the spectral ranges of the incident light, which can be absorbed by ZnO, CdS and $CuInS_2$, respectively. Note that $CuInS_2$ can also absorb the light of the green and red shades areas. The AM 1.5 solar spectrum is available from Ref. [NREL '08].

X Thermodynamic Data of Relevant Compounds

Values for the standard free enthalpies ΔH and standard entropies ΔS of various elements and binary compounds, which are relevant for the reactions discussed in this thesis. The standard enthalpy and standard entropy are defined as the changes in enthalpy and entropy, that accompany the formation of 1 mole of the respective substance from the elements.

Table X.1: Values for the standard free enthalpies ΔH and standard entropies ΔS of various elements and compounds, which are relevant for the reactions discussed in this thesis. ΔH and ΔS are given for temperatures of T = 298 K = 25 °C, T = 700 K = 423 ° C, T = 900 K = 627 °C. (G) indicates the gas phase. The values are taken from Ref. [Knacke '91].

Compound	**ΔH_{298K} [J·mol^{-1}]**	**ΔH_{700K} [J·mol^{-1}]**	**ΔH_{800K} [J·mol^{-1}]**	**ΔH_{900K} [J·mol^{-1}]**
Cu	0	10275	13001	15808
Cu_2S	-79496	-38523	-28763	-20298
CuS	-53718	-33680	Not stable	Not stable
CuS (G)	320494	335116	338814	942521
$InCl_3$	-537225	-494456	Not stable	Not stable
$InCl_3$ (G)	-376258	-344029	-335841	-327629
In_2O_3	-925919	-879222	-866738	-854085
In_2S_3	-355640	-303861	-289929	-275442
HCl (G)	-92307	-80515	-77497	-74438
H_2O (G)	-241856	-227283	-223333	-219287
H_2 (G)	0	11723	14698	17706
H_2S (G)	-20501	-5191	-978	3353

Compound	**ΔS_{298K} [J·K^{-1}mol^{-1}]**	**ΔS_{700K} [J·K^{-1}mol^{-1}]**	**ΔS_{800K} [J·K^{-1}mol^{-1}]**	**ΔS_{900K} [J·K^{-1}mol^{-1}]**
Cu	33.162	54.858	58.498	61.802
Cu_2S	120.918	209.217	222.329	232.299
CuS	66.526	108.817	Not stable	Not stable
CuS (G)	252.504	283.459	288.397	292.763
$InCl_3$	141.001	230.497	Not stable	Not stable
$InCl_3$ (G)	341.356	409.524	420.457	430.13
In_2O_3	104.182	202.035	218.702	233.602
In_2S_3	163.594	272.105	290.701	307.758
HCl (G)	186.908	211.898	215.926	219.529
H_2O (G)	188.824	219.368	224.641	229.405
H_2 (G)	130.679	155.545	159.518	163.06
H_2S (G)	205.757	237.786	243.409	248.516

XI Vibrations of the A_1, $B_2{}^1{}_{LO}$ and $E^1{}_{LO}$ Modes of Chalcopyrite-Type $CuInS_2$

In Fig. XI.1, the atomic movements of the atoms in chalcopyrite-type $CuInS_2$ for the vibrations of the A_1 (a), $B_2{}^1{}_{LO}$ (b) and $E^1{}_{LO}$ (c) Raman modes are visualized according to Ref. [Rudigier_1 '04]. It can be seen that in the A_1 mode, only the anion sublattice of $CuInS_2$ vibrates, whilst in the $B_2{}^1{}_{LO}$ and $E^1{}_{LO}$ Raman modes, atoms of all three species (copper, indium and sulfur) are involved in the vibration. Furthermore, for the $B_2{}^1{}_{LO}$ and $E^1{}_{LO}$ Raman modes, the vibrations of all participating atoms occur on one single axis, whereas the sulfur atoms vibrate in different planes in the A_1 mode.

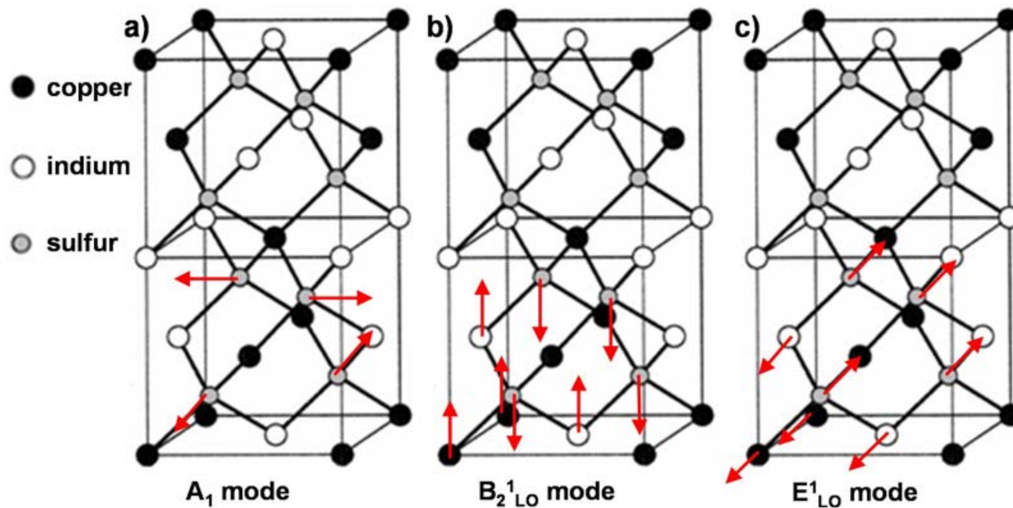

Fig. XI.1: Atomic movements of the A_1 (a), $B_2{}^1{}_{LO}$ for $\boldsymbol{q} \parallel$ z-axis (b) and $E^1{}_{LO}$ for $\boldsymbol{q} \parallel$ y-axis (c) Raman modes of chalcopyrite-type $CuInS_2$. For the sake of clarity, the movements are only indicated for the lower half of the crystal lattice. The sulfur atoms in the upper part vibrate analogously [Rudigier_1 '04].

XII Publications

The following publications have been published or submitted in the course of this thesis.

Journal Publications:

Parts of this work have already been published or submitted in the following articles:

- C. Camus, E. Rudigier, D. Abou-Ras, N. A. Allsop, T. Unold, Y. Tomm, S. Schorr, S. E. Gledhill, T. Köhler, J. Klaer, M. C. Lux-Steiner, Ch.-H. Fischer (2008): *"Phonon confinement and strain in $CuInS_2$"*, Applied Physics Letters, **92:** 101922

- C. Camus, N. A. Allsop, S. E. Gledhill, W. Bohne, J. Röhrich, I. Lauermann, M. C. Lux-Steiner, Ch.-H. Fischer (2008): *"Properties of Spray ILGAR $CuInS_2$ thin films"*, Thin Solid Films, **516-520:** 7026-7030

- C. Camus, N. A. Allsop, S.E. Gledhill, T. Köhler, I. Lauermann, W. Bohne, J. Röhrich, M. C. Lux-Steiner, Ch.-H. Fischer (2008): *"Initial Growth of Spray ILGAR $CuInS_2$ Thin Films"*, Applied Physics A: Materials & Processing, **submitted**

- C. Camus, D. Abou-Ras, N. A. Allsop, S.E. Gledhill, T. Köhler, I. Lauermann, J. Rappich, M. C. Lux-Steiner, Ch.-H. Fischer (2008): *"Morphology and Composition of Spray ILGAR $CuInS_2$ Thin Films"*, Applied Physics A: Materials & Processing, **submitted**

Further Journal Publications have been published or submitted in the course of this thesis:

- N. A. Allsop, C. Camus, A. Hänsel, S. E. Gledhill, I. Lauermann, M. C. Lux-Steiner, Ch.-H. Fischer (2007): *"Indium sulfide buffer/CIGSSe interface engineering: Improved cell performance by the addition of zinc sulfide"*, Thin Solid Films, **515:** 6068-6072

- S. Gledhill, A. Grimm, D. Greiner, W. Bohne, J. Röhrich, N. Allsop, C. Camus, M. Lux-Steiner, Ch.-H. Fischer (2008): *"Doping induced structural and compositional changes in ZnO spray pyrolysed films and the effects on optical and electrical properties"*, Thin Solid Films, **submitted**

- S. Gledhill, A. Grimm, N. Allsop, T. Koehler, C. Camus, M. Lux-Steiner, Ch.–H. Fischer (2008): *"A spray pyrolysis route to the undoped ZnO layer of Cu (In, Ga) (S, $Se)_2$ solar cells"*, Thin Solid Films, **submitted**

- H. Mönig, Ch. Jung, Ch.-H. Fischer, I. Lauermann, A. Grimm, C. Camus, C. A. Kaufmann, P. Pistor, T. Kropp, M. C. Lux-Steiner (2008): *"Controlled variation of the information depth by angle dependent soft x-ray emission spectroscopy: a study on polycrystalline $Cu(In,Ga)Se_2$"*, Applied Surface Science, **in press**

- T. Koehler, S. Gledhill, N. Allsop, C. Camus, A. Hänsel, W. Bohne, J. Röhrich, M. Lux-Steiner, Ch.-H. Fischer (2008): *"A technological investigation into ZnO films to allow up-scaling of the dip-ILGAR deposition process to a high through-put tape coater"*, Thin Solid Films, **submitted**

Conference Proceedings:

Parts of this work have been presented in an oral conference presentation and have been published in the respective conference proceedings:

- C. Camus, N. A. Allsop, T. Köhler, M. Krüger, S. E. Gledhill, J. Klaer, J. Rappich, M. C. Lux-Steiner, Ch.-H. Fischer (2008): *"Non-vacuum Chalcopyrite Solar Cell Absorbers: The Spray ILGAR Approach"*, Proceedings of the 33rd IEEE Photovoltaic Specialist Conference, San Diego: **in press**

Further publications in conference proceedings:

- N. A. Allsop, C. Camus, S. Gledhill, T. Unold, M. Lux-Steiner, T. Niesen, Ch.-H. Fischer (2007): *"Nanostructured ZnS:In_2S_3 Buffer Layers on Cu(In,Ga)$(S,Se)_2$: Can Voltage and Efficiency be Improved Through Interface Inhomogeneities on a Scale Below the Minority Carrier Diffusion Length?"*, Materials Research Society Symposium Proceedings, **1012:** Y02-03

- Sophie E. Gledhill, N. Allsop, P. Trier, C. Camus, M. Lux-Steiner, Ch.-H. Fischer (2007): *"Towards Lower Deposition Temperatures of Spray Deposited ZnO Films"*, Materials Research Society Symposium Proceedings, **1012:** Y02-10

Poster Presentations:

Parts of this work have been presented as a poster presentation at the respective conference:

- C. Camus, N. Allsop, S. Gledhill, D. Abou-Ras, I. Lauermann, T. Kropp, S. Fiechter, W. Bohne, J. Röhrich, M. Lux-Steiner, Ch.-H. Fischer (2007): *"A Systematic Study of the Deposition of Spray ILGAR $CuInS_2$ Thin Films for Photovoltaic Applications"*, Spring Meeting of the European Materials Research Society, Strasbourg, France

Further poster presentations at conferences:

- H. Mönig, M. Bär, C. Camus, A. Ennaoui, A. Grimm, C. Jung, C. Kaufmann, P. Körber, T. Kropp, I. Lauermann, S. Lehmann, M. Lux-Steiner, T. Münchenberg, P. Pistor, S. Puttnins, R. Saez-Araoz, H.-W. Schock, S. Sokoll, Ch.-H. Fischer (2007): *"Depth-profiling of thin film solar cell components by synchrotron excited soft X-ray emission spectroscopy"*, DPG Frühjahrstagung, Regensburg, Germany

- Ch.-H. Fischer, N. Allsop, C. Camus, S. Gledhill, M. C. Lux-Steiner, T. P. Niesen (2007): *"Efficient and stable CIGSSe Mini-Modules with Cd-free In_2S_3 Buffer Layers deposited by the in- line Spray-ILGAR® Process"*, 22nd European Photovoltaic Solar Energy Conference, Milan, Italy

- Ch.-H. Fischer, N. Allsop, C. Camus, A. Grimm, R. Klenk, T. Kropp, I. Lauermann, H. Mönig, P. Pistor, M. C. Lux-Steiner, M. Gorgoi, F. Schäfers, W. Braun (2007): *"Depth profiling of electronic properties in chalcopyrite thin film solar cell components by hard X-ray high kinetic energy photoelectron spectroscopy (HIKE)"*, 15th International Conference on Vacuum Ultraviolet Radiation Physics, Berlin, Germany